Characteristics and Optimization of a PMLSM for HTS Magnetic Suspension Propulsion System

L.H. Zheng, J.X. Jin, Y.G. Guo, W. Xu, H.Y. Lu, and J.G. Zhu

***Abstract*—Permanent magnet (PM) linear synchronous motors (PMLSMs) can be integrated with a high temperature superconducting (HTS) magnetic suspension system to be used in such as electromagnetic aircraft launcher and maglev transportation which have a levitated object moving on a long linear track. This paper presents the design and electromagnetic characteristic analysis of a long-primary single-sided PMLSM for a HTS bulk-PM guideway repulsion magnetic suspension propulsion system. Based on the characteristics and performance analysis of the PMLSM, a new type of HTS suspension propulsion system driven by a double-sided PMLSM with an optimal PM structure is then proposed. The running characteristics of the linear propulsion systems are studied through finite element analysis (FEA) with comprehensive performance results obtained for practical development.**

***Keywords*—High temperature superconductor (HTS), Permanent magnet linear synchronous motor (PMLSM), Electromagnetic simulation, HTS bulk, HTS magnetic suspension.**

1. Introduction

Permanent magnet linear synchronous motor (PMLSM) technology has a rapid development in recent years, which results PMLSM increasingly used as actuators in industrial drive applications, such as computer controlled machining tools, X-Y driving devices, robots, semiconductor manufacturing equipment, transportation and suspension propulsion system. When a PMLSM is applied into the magnetic suspension propulsion system like maglev, HTS bulk-PM guideway repulsion type suspension system can be integrated due to stable levitation force and guidance force–simultaneously generated between PMs and HTS bulks [1-3]. The main advantages of HTS magnetic suspension system is the strong levitating force with passive and self-stabilizing feature, leading to the simplification of the sophisticated control system for regulating the length of air gap, which is necessary for other types of levitation transportation systems.

Manuscript received April 5, 2010; revised June 8, 2010.

This work was supported by the Chinese High-Tech R&D (863) Program under Grant No. 2007AA03Z208.

J. X. Jin, and L. H. Zheng are with School of Automation, University of Electronic Science and Technology of China, Chengdu 611731, China (e-mail: jxjin@uestc.edu.cn, zluhai@uestc.edu.cn).

Y. G. Guo, W. Xu, H. Y. Lu, and J. G. Zhu are with Faculty of Engineering and Information technology, University of Technology Sydney, Sydney, Australia (e-mail: youguang@eng.uts.edu.au).

In this work, a HTS magnetic suspension propulsion system having a long-primary single-sided moving-magnetic type PMLSM for driving has been developed, which has lightweight of secondary mover and able to realize higher force density and acceleration capability in shorter time. The HTS magnetic suspension system consists of HTS bulks put in cryogenic vessels on the mover and PM guideways installed on both sides of PMLSM stator. The electromagnetic characteristics and performance of the PMLSM are studied by numerical analysis and finite element analysis (FEA) methods. Based on the results, an optimal HTS suspension propulsion system drived by a double-sided PMLSM is proposed with its performance characteristic analysis.

2. Model of HTS Magnetic Suspension Propulsion System

The structure model of the HTS magnetic suspension propulsion system composed of a PMLSM and HTS bulks-PM guideway repulsion suspension sub-structure is shown in Fig. 1. The primary stator of the PMLSM is composed of three-phase copper windings and an iron core, while the secondary is made up of PMs and a piece of back iron. Table 1 lists the major parameters of the PMLSM.

The HTS magnetic suspension systems are fitted on both sides of the PMLSM, and the PM-guideways are consisted of PMs and magnetic iron (Fe) ribs assembled as shown in Fig. 2. The magnetization directions of left-side and right-side PMs are along the vertical direction, and the middle PMs are installed with opposite magnetization direction. The iron core is put in the middle of PMs to concentrate magnetic field for generating stronger magnetic field on the upper surface of PM-guideways and weaker magnetic field on the lower surface.

The HTS bulks-PM guideway repulsion suspension system can realize self-levitation and self-guidance, so that the PMLSM can run without any sliding friction force and any assistant guidance control system.

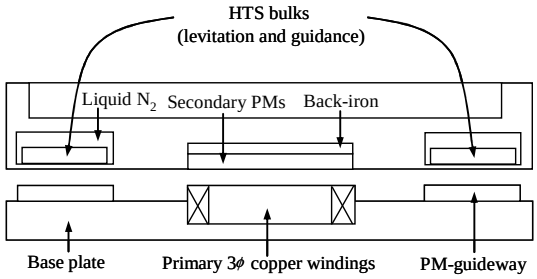

Fig. 1. Model of HTS suspension propulsion system drived by a single-sided PMLSM.

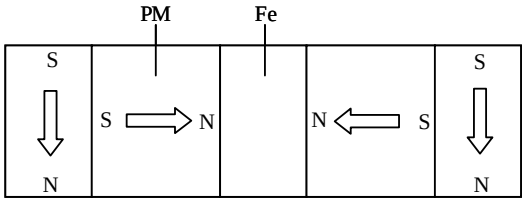

Fig. 2. PM guideway structure.

Table 1. Major dimensions and parameters of PMLSM

Item	Values
Primary	
Copper windings	
Number of turns N_1	200
Diameter of copper wire (mm)	1.18
Resistivity (Ω·m)	1.75E-8
Iron core	
Tooth length (movement direction) (mm)	10
Tooth depth (mm)	100
Slot width (mm)	20
Tooth pitch y_1 (mm)	30
Pole pitch τ (mm)	45
Number of slots	37
Main air gap g (mm)	4
Secondary	
PM	
PM length (movement direction) l_s (mm)	45
PM width w_s (mm)	45
PM height h_s (mm)	12
PM trapping field B (T)	0.5
Number of PMs (movement direction)	6
Back iron thickness H_{back} (mm)	10
Running parameters	
Frequency (Hz)	5
Phase voltage (V)	106
Phase current (A)	6.8
Phase resistance (Ω)	13.5
Maximum thrust force (N)	254

3. Numerical Analysis

3.1 PM Flux Linkage and Back EMF

The transverse section and longitudinal section of the PMLSM are shown in Fig. 3. The length of PMs l_s is equal to the pole pitch τ with no gap between them. Neglecting the magnetic resistance of primary iron-core and secondary back-iron, the magnetic flux linkage of one coil generated by one pole-pair of PMs can be obtained approximately as

$$\begin{aligned}\psi_{\mathrm{PM}} &= \frac{\mathcal{F}}{R_{\mathrm{tot}}} = \frac{H_c \cdot h_s}{h_s/\mu_r\mu_0 l_s w_s + g/\left[\mu_0 \cdot (l_s + l_t)/2 \cdot (w_s + w_t)/2\right]} \\ &= \frac{\mu_0 H_c h_m l_m w_m (l_s + l_m)(w_m + w_s)}{4g l_m w_m + h_m l_m w_m + h_m l_m w_s + h_m l_s w_m + h_m l_s w_s}\end{aligned} \quad (1)$$

where $\mathcal{F}$ is the magnetomotive force of magnetic circuit, R_{tot} the total magnetic reluctance, R_s the magnetic reluctance of PM, R_g the magnetic reluctance of air-gap, μ_r the relative permeability of PM, H_c the magnetic field intensity of PM, μ_0 ($4\pi\times10^{-7}$ H/m) the permeability of vacuum; l_s, w_s, and h_s are the length, width and height of PM respectively; l_t, w_t the length and width of stator-tooth respectively. When the parameters are substituted in (1), the ψ_{PM} can be calculated out with the value of 0.4 Wb.

When the secondary rotor moves, an electromotive force (EMF) is induced in the stator windings. By differentiating the PM flux of phase winding against time, the back EMF is determined with an rms value as

$$E_0 = \frac{1}{\sqrt{2}}\frac{\pi}{\tau} N_1 k_N \psi_{\mathrm{SC}} v_s = k_E v_s \quad (2)$$

where $k_E = \frac{1}{\sqrt{2}}\frac{\pi}{\tau} N_1 k_N \psi_{\mathrm{SC}}$ is the back EMF constant, τ the pole pitch, N_1 the number of turns of winding, and k_{N} the winding factor.

Neglecting the magnetic reluctance of stator core, the magnetic reluctance of the closed circuit in which the magnetic flux flows generated by one coil can be calculated as

$$R_{tot} = \frac{y_1}{2\mu_0 A_c} \quad (3)$$

where A_{c} is the area of stator teeth, A_{c} = 1500 mm^2. So that the inductance L of one coil can be calculated by

$$L = \frac{N_1\phi}{i} = \frac{N_1^2}{R_{tot}} \quad (4)$$

where N_1 = 200, L = 5 mH. There are 12 coils for one-phase, so the one-phase coil inductance is L_1 = 60 mH.

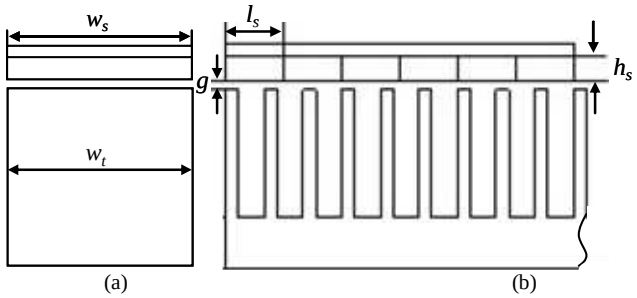

Fig. 3. Model of PMLSM. (a) Transverse section; (b) Longitudinal section.

3.2 Thrust and Normal Forces

In 2D plane magnetic field analysis, the thrust force F_{em} and normal force F_{n} have been expressed as [4]

$$F_{\mathrm{em}} = \oint_S \left[\frac{1}{2\mu_0}\left(B_x^2 - B_y^2\right)n_x + 2n_y B_x B_y\right] dS \quad (5)$$

$$F_n = \oint_S \left[\frac{1}{2\mu_0}\left(B_y^2 - B_x^2\right)n_y + 2n_x B_x B_y\right] dS \quad (6)$$

where S is the integrative path surrounding the moving part of the motor in the air-gap, B_{x} and B_{y} are the components along tangential and normal direction, respectively; n_{x} is the tangential vector per unit and n_{y} are normal vector per unit.

For the long-primary PMLSM, the stator copper loss cannot be neglected. The PMLSM has the characteristics of $X_{\mathrm{d}} = X_{\mathrm{q}} = X_{\mathrm{t}} = 2\pi f L_1$ [5], therefore the electromagnetic power can be derived as follows

$$P_{em} = \frac{3E_0}{R_1^2 + X_t^2}\left[U\left(X_t \sin\theta + R_1 \cos\theta\right) - E_0 R_1\right] \quad (7)$$

The electromagnetic thrust force is

$$F_{em} = \frac{P_{em}}{v_s} = \frac{3E_0\left[U\left(X_t \sin\theta + R_1 \cos\theta\right) - E_0 R_1\right]}{2\tau f\left(R_1^2 + X_t^2\right)} = \frac{3E_0\left[U\sqrt{R_1^2 + X_t^2}\sin\left(\theta + \phi\right) - E_0 R_1\right]}{2\tau f\left(R_1^2 + X_t^2\right)} \quad (8)$$

where $\phi = \arctan R_1 / X_t$. When θ = 90°- $\arctan R_1 / X_t$, the maximum thrust force $F_{\text{em\_max}}$ is

$$F_{\text{em\_max}} = \frac{3E_0\left(U\sqrt{R_1^2 + X_t^2} - E_0 R_1\right)}{2\tau f\left(R_1^2 + X_t^2\right)} \quad (9)$$

where R_1 is the phase resistance, X_t the synchronous reactance, U the phase voltage, θ the power angle, v_s the synchronous velocity, and $v_s = 2\tau f$, where f the frequency.

4. Levitation and Guidance Forces

The levitation force and guidance force are generated based on the shielding force and the pinning force of HTS bulks [6]. When the materials and dimensions of HTS bulk-PM are properly chosen, an appropriate levitation force and guidance force can be generated to levitate and guide the mover.

The levitation force and guidance force are the product of an external magnetic field and a shielding current flowing in a HTS bulk, and can be calculated by the following equations

$$F_{\text{Lev}} = \int_0^{TH}\int_{L/2}^{L/2-\delta}\int_{W/2}^{W/2-\delta} J_c \times B_x \,\mathrm{d}x\mathrm{d}y\mathrm{d}z \quad (10)$$

$$F_{\text{Gui}} = \int_0^{TH}\int_{L/2}^{L/2-\delta}\int_{W/2}^{W/2-\delta} J_c \times B_z \,\mathrm{d}x\mathrm{d}y\mathrm{d}z \quad (11)$$

where F_{Lev} is the levitation force, F_{Gui} the guidance force, J_c the critical current density, B_x the field along the transverse direction, B_z the field along the vertical direction; W, L and TH are the width, length and thickness of the HTS bulk, respectively; and δ the depth of field penetration. Here, it is assumed that induced shielding currents flowing in the bulk body are equal to the critical currents. The δ used as integral range is given by the following relation [7]

$$\delta = \frac{B_z - B_{\text{zfc}}}{\lambda \mu_0 J_c} \quad (12)$$

where B_{zfc} is the trapped magnetic field, λ the Nagaoka coefficient determined by the configuration of a sample. The Fig. 4 shows the interaction between a HTS bulk and the PM-guideway, and the Fig. 5 and Fig. 6 are the distributions of B_x and B_z for different heights h from upper surface of PM-guideway, respectively.

The levitation force versus the distance between a HTS bulk and the PM-guideway can be described with an exponential function as follows [8]

$$\begin{cases} F = F_{\text{Lev\_1}}\exp\left(-z/\alpha_1\right) - F_{\text{Att\_1}}\exp\left(-z/\beta_1\right) & move-towards \\ F = F_{\text{Lev\_2}}\exp\left(-z/\alpha_2\right) - F_{\text{Att\_2}}\exp\left(-z/\beta_2\right) & move-away \end{cases} \quad (13)$$

where $F_{\text{Lev\_1}}$ and $F_{\text{Att\_1}}$ are the levitation force and attractive force when the HTS bulk is moved towards the PM-guideway, respectively; $F_{\text{Lev\_2}}$ and $F_{\text{Att\_2}}$ are the levitation force and attractive force when the HTS bulk is moved away from the PM-guideway, respectively; α_1, α_2, β_1 and β_2 are constants, which are closely related to the superconductor and the distribution of magnetic field; z the distance between the HTS bulk and PM-guideway. Fig. 7 shows the levitation force characteristic versus the distance of HTS bulk to the PM-guideway.

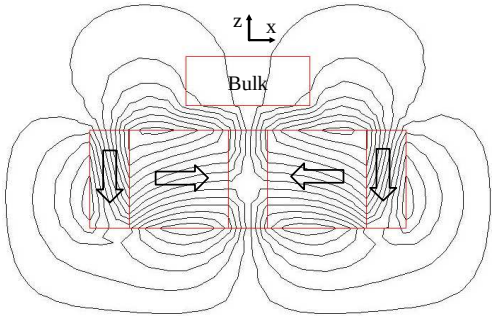

Fig. 4. Model of interaction between a HTS bulk and the PM guideway.

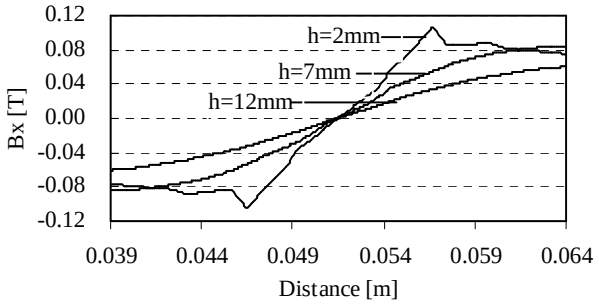

Fig. 5. Distributions of B_x for different heights.

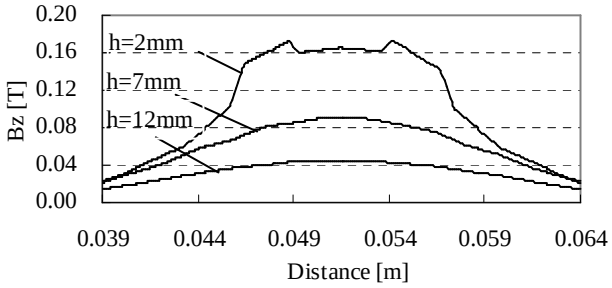

Fig. 6. Distributions of B_z for different heights.

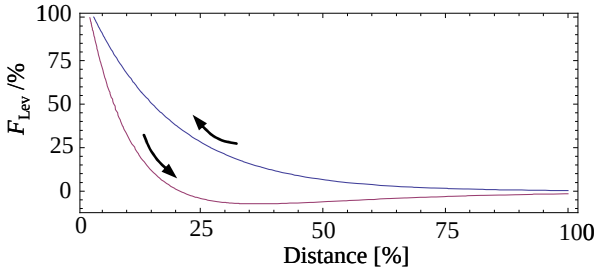

Fig. 7. The levitation force characteristics between a HTS bulk and the PM-guideway.

5. Performance Analysis

5.1 FE Model

According to the geometric parameters of PMLSM, a 2D FE model is built, which is sufficient for the theoretical analysis with relatively low computational complexity. The FE model is shown in Fig. 8 with the materials in model are numbered as: ① PM North (with the magnetization direction along the negative y-axis direction); ② PM South (with the magnetization direction along the y-axis direction); ③ PM back iron; ④ Band; ⑤ Stator iron core; and ⑥ Copper stranded coils.

The magnetic vector potentials obey the periodical boundary conditions on the y-direction boundary lines of the primary stator and band. The time-stepping transient analysis is applied to resolve. The analysis results of the no-load, start-up, detent force, thrust force and normal force characteristics of the PMLSM are detailed as follows.

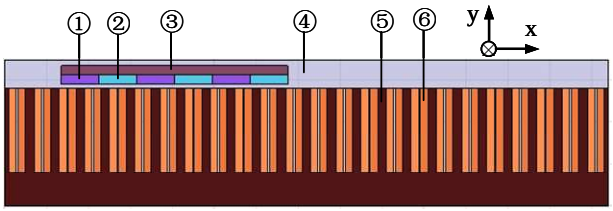

1-PM North, 2-PM South, 3-Back iron, 4-Band, 5-Iron core, 6-Coils.
Fig. 8. FE model of the PMLSM.

5.2 No-Load Analysis

In 2D transient simulation at no-load without any excitations, the back electromagnetic force (EMF) and PM flux linkage can be calculated. Set the secondary rotor move with a constant speed as $v = 2f\tau = 450$ mm/s, where $f = 5$ Hz, $\tau = 45$ mm. The time stop of simulation is 1 s, and the time step is 0.01s.

After simulating, the three-phase induced current and back EMF is obtained as shown in Fig. 9 and Fig. 10, respectively. As can be seen from the figures, the amplitude of induced current is $I_m = 0.82$ A, and the back EMF is $E_0 = 12$ V. Fig. 11 shows the three-phase flux linkage characteristics with the same amplitude of $\psi_{PM} \approx 0.4$ Wb but are shifted by 120^o electrical to each other.

By comparing the phases of the flux linkage, induced voltage and induced current, it is found that the three-phase induced currents have 120 electrical degrees delay after those of the induced back EMF, and which are also 120 electrical degrees delay to the flux linkages.

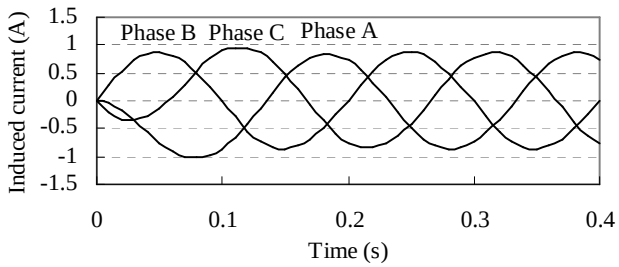

Fig. 9. Three-phases current characteristics.

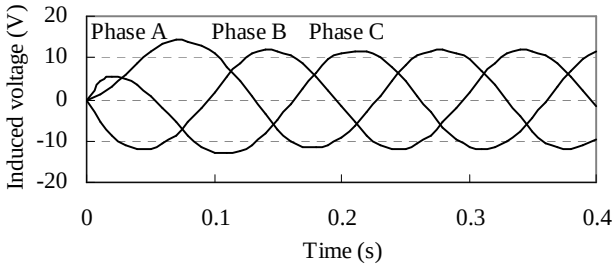

Fig. 10. Three-phases induced back EMF.

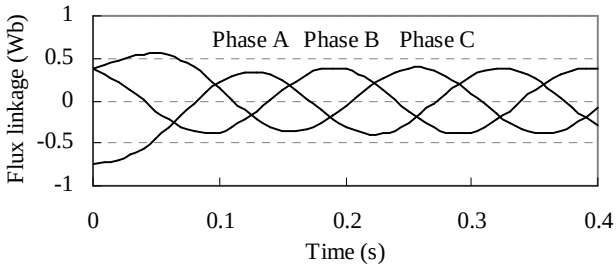

Fig. 11. Three-phases flux linkage characteristics.

5.3 Detent Force Analysis

The slotted PMLSM has a detent force F_d due to the interaction of the secondary PMs with the primary slotted core, and the detent force includes the cogging force and end force. For the long-primary moving-magnetic type PMLSM, the end force can be neglected. The detent force is generally undesired effect that contributes to the force ripple and vibration of motor. So it is necessary to realize the detent force characteristic and minimize it.

The detent force can be approximately obtained by measuring the force while setting the secondary mover move at a very low constant velocity at no-load. In the simulation, a constant velocity of 4.5 mm/s is applied with the result is shown in Fig. 12. From the results, it is found that the pole arc coefficients α_i has important influence on the detent force. As can be seen from the waveforms, the detent force wave shows a periodic fluctuation with the period length equal to 30mm, which is equal to the tooth pitch y_1. The amplitudes of detent force vary with the α_i. When $a_i = 1$, the amplitude is about ±28N as shown in Fig. 12(a), and Fig. 12(b) shows that the plus-minus amplitudes change to 5.6 N and -8.5 N when $a_i = 0.75$, respectively. The average amplitude of detent force F_{d_avg} versus different α_i is calculated as shown in Fig. 13. It is concluded that it has a maximum amplitude of detent force at $\alpha_i = 1$ when the length of PM equal to the pole pitch τ. When the α_i is selected between 0.75-0.875, it will have a relative small detent force.

Similarly, the normal force F_d also has the period characteristic like detent force as the results shown in Fig. 14 with the maximum fluctuation amplitudes of 43 N and 22.1 N for $\alpha_i = 1$ and $\alpha_i = 0.75$, respectively. It is can be thought that the tangential component of the fluctuation value of normal force lead to the detent force, and the detent force can be eliminated when the non-salient pole is adopted.

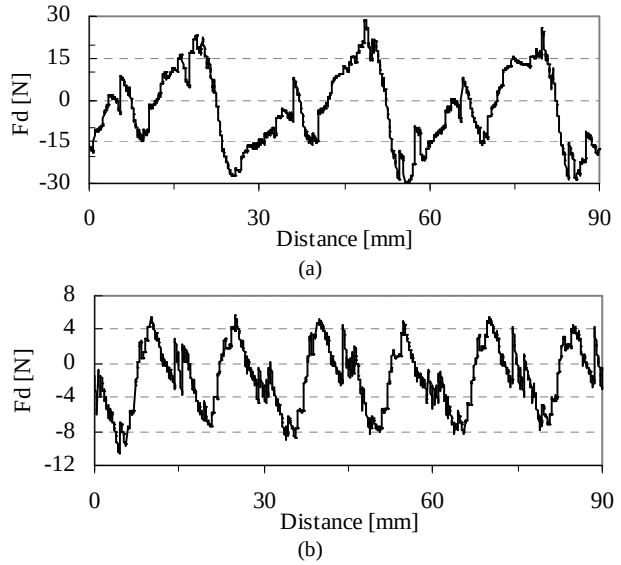

Fig. 12. Detent force characteristic vs. different pole arc cofficient α_i, (a) α_i=1, (b) α_i=3/4.

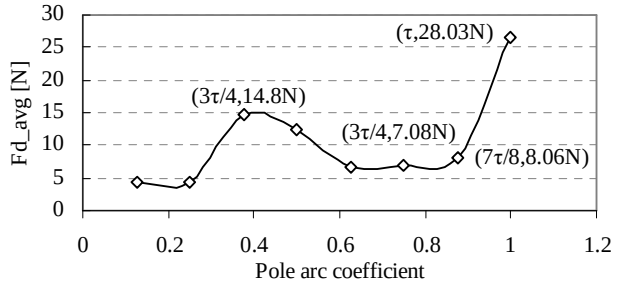

Fig. 13. Average amplitude of detent force F_{d_avg} vs. α_i.

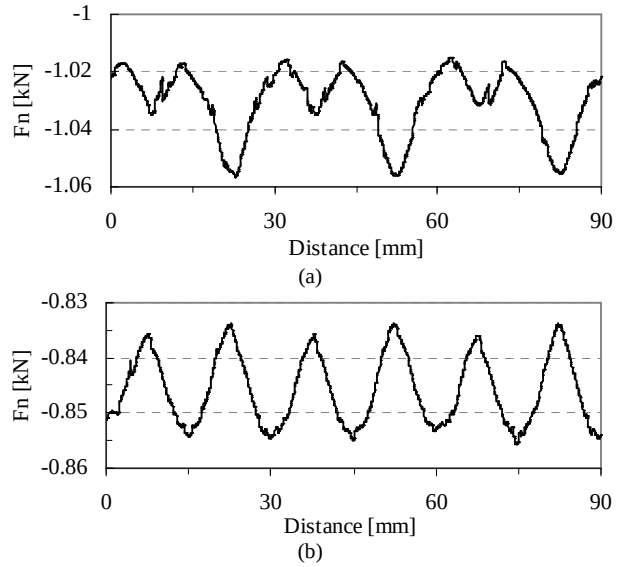

Fig. 14. Normal force F_n characteristic vs. distance for different α_i. (a) α_i=1; (b) α_i=3/4.

5.4 Start-Up Characteristics

In load analysis, the three-phase voltages are excited as

$$U_a = \sqrt{2}U\sin(2\pi ft + \theta_0) \tag{14}$$

$$U_b = \sqrt{2}U\sin(2\pi ft + \theta_0 - 2\pi/3) \tag{15}$$

$$U_c = \sqrt{2}U\sin(2\pi ft + \theta_0 - 4\pi/3) \tag{16}$$

where U is the amplitude of phase voltage, θ_0 the initial phase angle. The main dynamic simulation parameters with the values based on the actual prototype and calculation are listed in Table 2.

Fig. 15 shows the start-up thrust force characteristics at no-load with the initial position of the axis of phase A coinciding with the d-axis. As can be seen from Fig. 15(a), a great thrust pulsation is generated at the initial stage with the maximum amplitude of 367 N, and tends to steady state 0.6 s later with a force ripple of ±30 N as shown in Fig. 15(b), which is approximately equal to the amplitude of detent force as shown in Fig. 12(a), which verifies that the force ripple is mainly caused by the detent force.

The start-up speed and position characteristics are shown in Fig. 16(a) and Fig. 16(c). The velocity pulsation is caused by the thrust pulsation, and he maximum overshoot is 205%. After 0.6 s, the motor reaches a steady state in a mean running velocity of 0.45 m/s with the velocity ripple about ±0.04 m/s as shown in Fig. 16(b), and the mean velocity is equal to the synchronous velocity of $2f\tau$. Under this speed, the displacement is 682.7 mm after 1.5 s.

Initial position x_0 has important influence on the start-up performance. Fig. 17 shows the start-up characteristic of PMLSM for different positions with the value of 0, $\tau/2$, $3\tau/4$, $3\tau/2$, and $7\tau/4$. As can be seen from Fig. 17, when $x_0 = \tau/2$, it has the smallest thrust pulsation, but when $x_0 = 3\tau/4$ and $3\tau/2$, a shift in the reverse direction is generated instantaneously, which degrades the start-up performance.

Fig. 18 and Fig. 19 show the influence of load force and load weight on the start-up of PMLSM at different initial positions, respectively. As can be seen from the figures, the motor can start normally when the load force $|F_L| \le 140$ N at $x_0 = 0$, and the maximum load force can reach 300N at $x_0 = \tau/2$ shown in Fig. 18(b), which is 2.1 times that of the former. Fig. 19(b) shows that the maximum load weight mass = 60 kg at $x_0 = 0$, and it reaches a value of 145 kg at $x_0 = \tau/2$, which is 2.4 times that of the former.

Table 2. Major Parameters of Dynamic Simulation

Parameters	Quantities	Parameters	Quantities
Mass	8.5 kg	Voltage U_m	106 V
Load force	0 N	Phase resistance R_1	13.5 Ω
Initial velocity	0 m/s	Inductance L_1	60 mH
Damping D_v	0 N·s/m	Time stop	1 s
Frequency	5 Hz	Time step	0.01 s

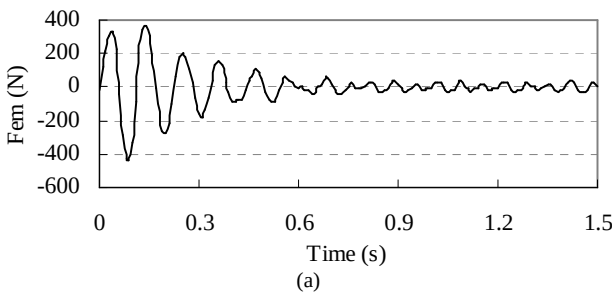

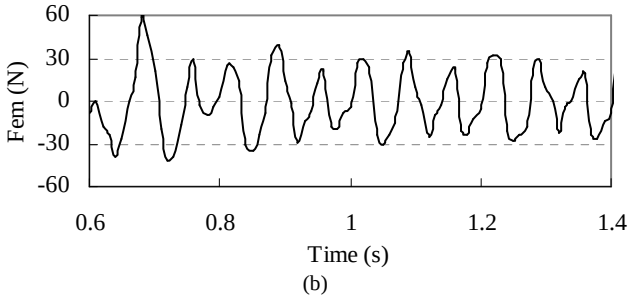

Fig. 15. Start-up force characteristic at no-load. (a) Thrust force F_{em} vs. time; (b) Force ripple vs. time.

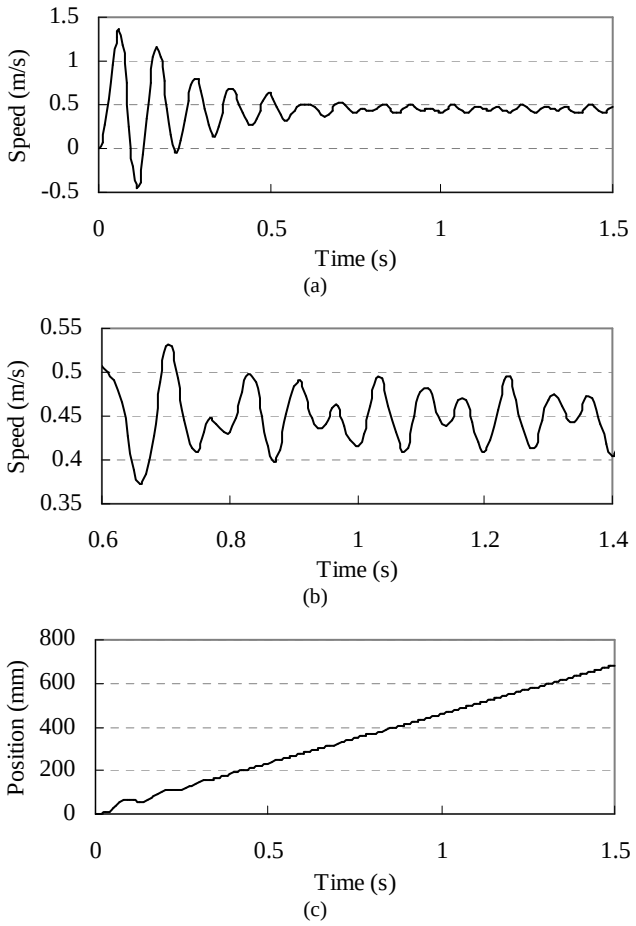

Fig. 16. Start-up characteristics at no load. (a) Speed vs. time; (b) Speed ripple; (c) Position vs. time.

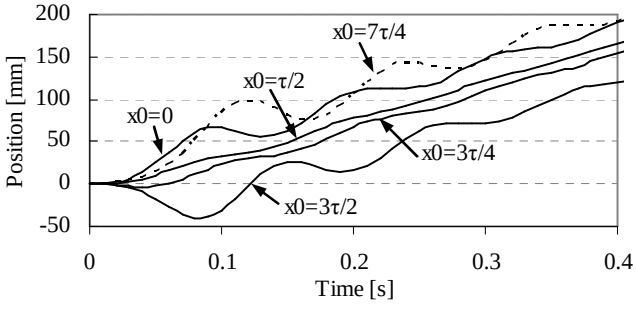

Fig. 17. Start-up characteristic vs. initial position x_0.

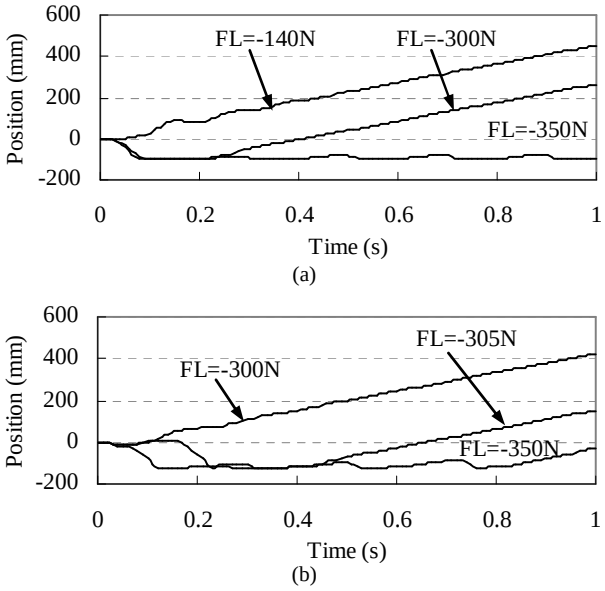

Fig. 18. Start-up characteristics vs. different load force. (a) $x_0 = 0$; (b) $x_0 = \tau/2$.

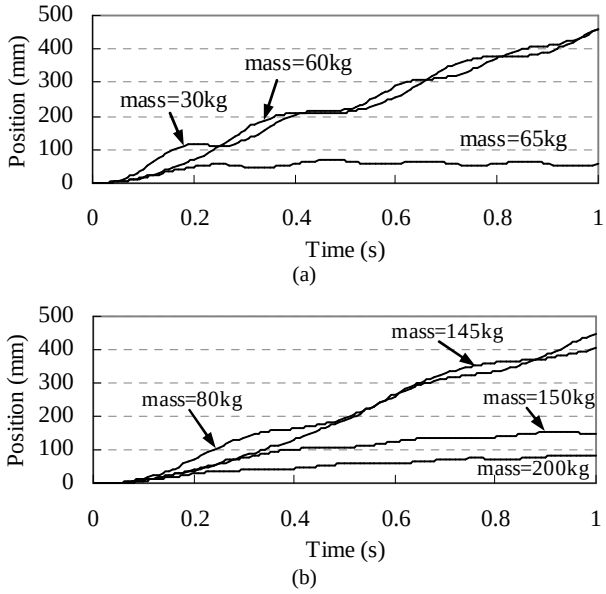

Fig. 19. Start-up characteristics vs. different load weight. (a) $x_0 = 0$; (b) $x_0 = \tau/2$.

5.5 Thrust and Normal Forces Characteristics

The $F_{em} = f(\theta)$ is an important characteristic for the PMLSM. Fig. 20 shows the locked-rotor thrust force characteristic for f = 5 Hz, and it is just the force-angle characteristic. As can be seen from it, when θ = 54°, the maximum locked-rotor thrust force is 399 N, and it is equal to the maximum thrust force F_{em_max}. The F_{em_max} decreases with the frequency of exciting voltage with the result shown in Fig. 21.

The magnetic flux density B of PM and exciting current have direct effects on thrust force and normal force. Fig. 22 shows the F_{em_max} and average normal force F_{n_avg} versus B. As can be seen from the figure, the F_{em_max} and F_{n_avg} increase nearly linearly with B. The ratio of F_{n_avg}/F_{em_max} is between 1.59-5.96 when the B = 0.3-1.2 T. Similarly, the

F_{em_max} and F_{n_avg} increase with the exciting current nearly linearly as shown in Fig. 23, and the ratio of F_{n_avg}/F_{em_max} is between 6.89−1.76 when the exciting current I = 3.2-46.2 V. It is concluded that improving the exciting current has a better effect to increase the thrust force with lower F_{n_avg}/F_{em_max}.

The shape and size of PM have non-ignorable influences on F_{em}. Fig. 24 shows the F_{em_max} vs. thickness of PM for different exciting voltage, and it can be seen that the F_{em_max} will tend to saturate with the thickness of PM increasing to 20 mm for different exciting voltages.

The pole arc coefficient a_i also has important effects on F_{em}, and it has an optimal value to realize an optimal thrust force. As can be seen from Fig. 25, the F_{em_max} increases with a_i until the value equal to 0.875, then the thrust force will decrease with the a_i till a_i = 1 where the F_{em_max} is smaller than that at a_i = 0.75. The curve of F_{em_max} /F_d versus the a_i shows that it reaches a peak value at a_i = 0.75. It is concluded that it will reach an optimal thrust force with lower force ripple generated by detent force when the a_i = 0.75.

The influence of the number of secondary PM poles N_{PM} on the F_{em} is calculated as shown in Fig. 26. As can be seen from it, the thrust force increase linearly with the number of poles when N_{PM} < 7. When $N_{PM} \geq 7$, the thrust force will reach saturation with the mean F_{em_max} = 450 N.

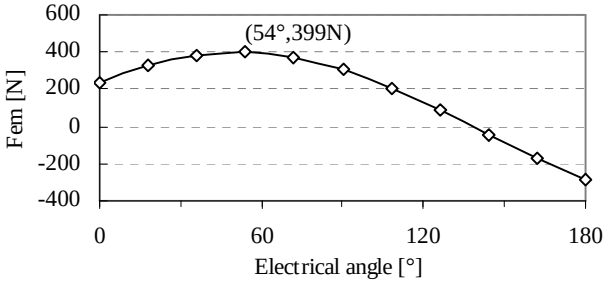

Fig. 20. Locked-rotor F_{em} characteristic.

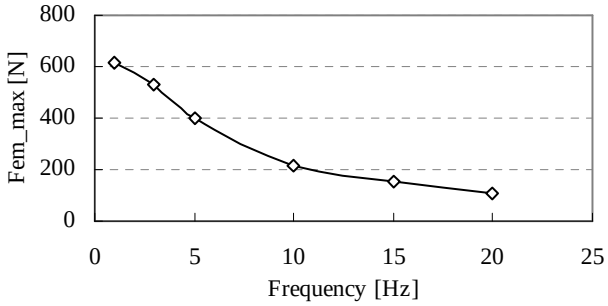

Fig. 21. F_{em_max} vs. frequency of exciting voltage.

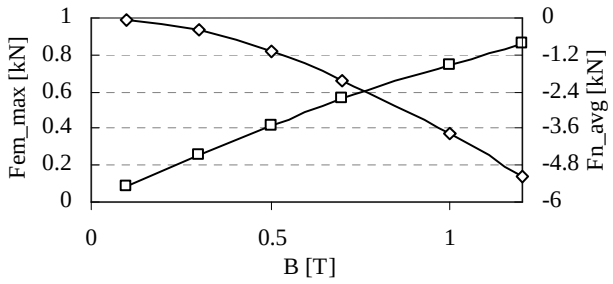

Fig. 22. F_{em_max} and F_{n_avg} vs. different B of PM.

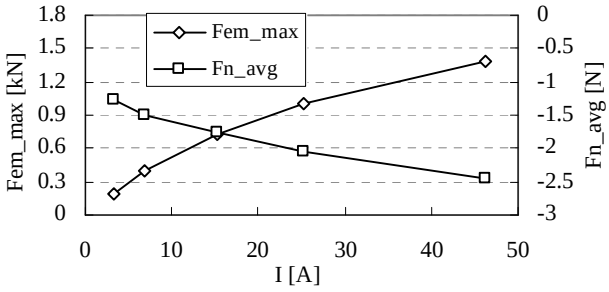

Fig. 23. F_{em_max} and F_{n_avg} vs. different current.

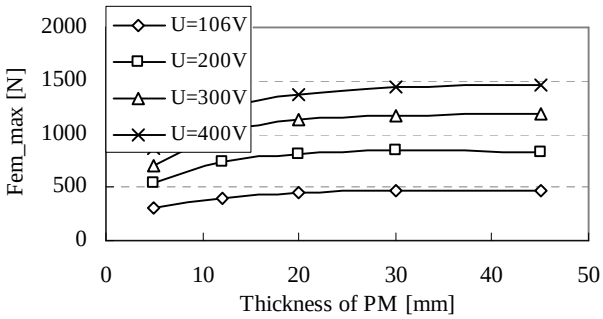

Fig. 24. F_{em_max} vs. different thickness of PM.

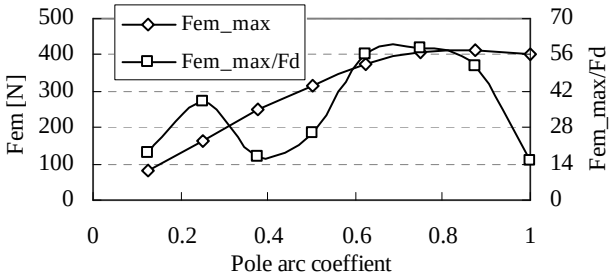

Fig. 25. F_{em_max} vs. pole arc coefficient and the F_{em_max}/F_d characteristics.

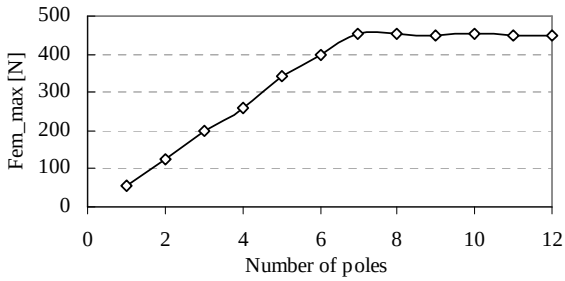

Fig. 26. F_{em_max} vs. the number of poles of PM.

6. Optimal Design

Based on the analysis above, it can be seen that the normal force between the primary stator and PM-secondary is great, and it is about 1.6～6.9 times the thrust force, which counteracts the levitation force generated by HTS bulk-PM guideway suspension sub-system and leads to decrease the load capacity. In this work, an optimization design is carried out with a new HTS suspension propulsion system is proposed, which is drived by a long-primary double-sided PMLSM with a novel integrated model as shown in Fig. 27.

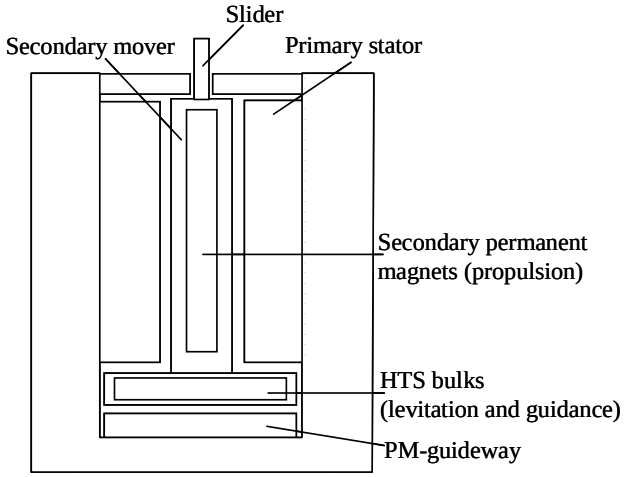

Fig. 27. A new design of HTS suspension propulstion system drived by a double-sided PMLSM.

In the double-sided design, the normal attraction forces produced by the motor can be mostly cancelled, and the thrust force will be double as the single-sided one. The HTS suspension unit is installed underneath the secondary mover, which only needs to support the weight of mover and load. In order to confirmation the performance of the propulsion system, the primary stator used in the previous single-sided one is adopted in the double-sided model. The optimal dimensions of the PMs are listed in Table 3 with the running parameters and performance features.

Fig. 28 shows the start-up thrust force characteristics at no load. Fig. 29 shows the thrust force F_{em} versus the electrical angle θ. As can be seen from it, the maximum thrust force F_{em_max} are approximately 2 kN at θ = 54°. From the F_{em_max} vs. load force characteristics shown in Fig. 30, the maximum start-up thrust force at $x_0 = \tau/2$ can be achieved as about 1050 N, which is 3.5 times that of the single-one, and the maximum start-up force in place can reach 1.3 kN.

Fig. 31 shows the characteristic of F_{em} vs. load weights. It is shown that the maximum load weight is 560 kg, which is 3.8 times that of the single-sided one. Without the influence of normal force, the secondary mover with the load can be levitated by HTS magnetic suspension system easily.

Table 3. Optimal parameters of double-sided PMLSM

Item	Values
PM	
PM length (mm)	33.75
Pole arc coefficient	0.75
PM width w_s (mm)	45
PM height h_s (mm)	25
PM trapping field B (T)	0.7
Number of PMs (movement direction)	6
Running parameters	
Frequency (Hz)	5
Phase voltage (V)	200
Phase resistance (Ω)	13.5
Performance	
Maximum load mass (kg)	560
Maximum thrust force (N)	2000
Maximum start-up thrust force (N)	1300

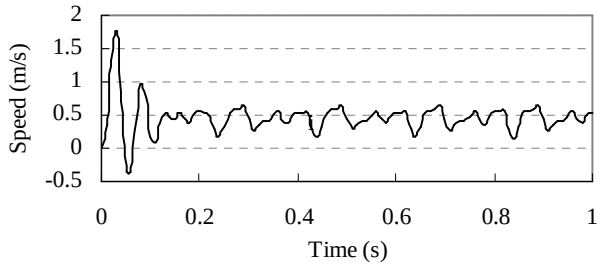

Fig. 28. Start-up thrust force characteristic at no load.

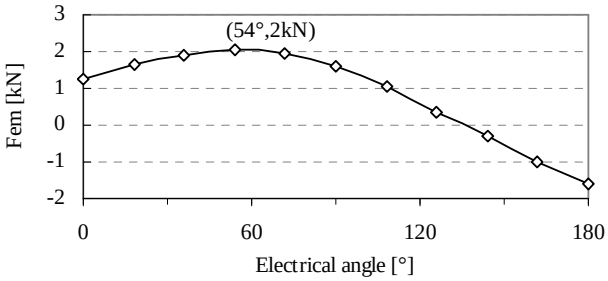

Fig. 29. F_{em} vs. electrical angle.

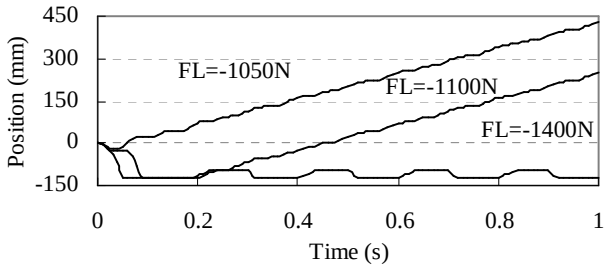

Fig. 30. Start-up characteristics vs. different load force at $x_0=\tau/2$.

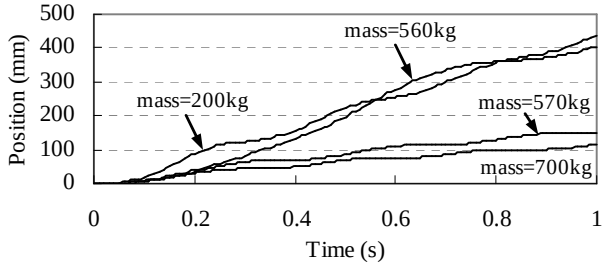

Fig. 31. Start-up characteristics vs. different load weight at $x_0=\tau/2$.

7. Conclusions

A prototype of HTS magnetic suspension propulsion system derived by a single-sided PMLSM is developed. The characteristics and performance analysis of the PMLSM show that it has an optimal pole arc coefficient to obtain a minimum detent force which minimizes the force ripple. The initial position has influences on start-up performance, and the maximum start-up load capacity has difference at different position. It also has an optimal thickness and poles of PM for different exciting voltage to obtain a saturation thrust force. In order to eliminate the influence of normal force, a new HTS suspension propulsion system driven by a double-sided PMLSM with an optimal secondary is proposed, and the performance characteristic analysis of which shows that it has comprehensive performance for the practical application.

References

[1] J. X. Jin, "High T_c superconductor theoretical models and electromagnetic flux characteristics," Journal of Electronic Science and Technology of China, vol. 4, no. 3, pp. 202-208, September 2006.

[2] J. X. Jin, and L. H. Zheng, "Verification of levitation force between a HTS and a permanent magnet," Physica C, vol. 460-462, pp. 1457-1458, 2007.

[3] Y. G. Guo, J. X. Jin, L. H. Zheng, J. G. Zhu, and H. Y. Lu, "A permanent magnet linear synchronous motor drive for HTS maglev Transportation Systems," Journal of Electronic Science and Technology of China, vol. 6, no. 2, pp. 125-129, June 2008.

[4] I. S. Jung, S. B. Yoon, J. H. Shim, and D. S. Hyun, "Analysis of forces in a short primary type and a short secondary type permanent magnet linear synchronous motor," IEEE Transactions on Energy Conversion, vol. 14, no. 4, pp. 1265-1270, 1999.

[5] Z. Deng, I. Boldea, and S. Nasar, "Forces and parameters of permanent magnet linear synchronous machines," IEEE Transactions on Magnetics, vol. 23, no. 1, pp. 305-309, 1987.

[6] J. X. Jin, "High T_c superconductor theoretical models and electromagnetic flux characteristics," Journal of Electronic Science and Technology of China, vol. 4, no. 3, pp. 202-208, September 2006.

[7] T. Suzuki, S. Araki, K. Koibuchi, K. Ogawa, K. Sawa, K. Takeuchi, M. Murakami, K. Nagashima, H. Seino, Y. Miyazaki, N. Sakai, I. Hirabayashi, and Y. Iwasa, "A study on levitation force and its time relaxation behavior for a bulk superconductor-magnet system," Physica C, vol. 468, no. 15-20, pp. 1461-1464, 2008.

[8] F. C. Moon, K. C. Weng, and P. Z. Chang, "Dynamic magnetic forces in superconducting ceramics," Journal of Applied Physics, vol. 66, pp. 5643-5645, 1989.

Lu Hai Zheng was born in Zhejiang, China in 1980. He received B.E. degree from Huaiyin Teachers College in 2005. He is currently pursuing the Ph.D. degree with University of Electronic Science and Technology of China. His research direction is high temperature superconducting linear machine technology, and control technology.

Jian Xun Jin received his B.E. in 1985 from Beijing University of Science and Technology, China; M.S. in 1995 from University of NSW, Australia; and Ph.D. in 1998 from University of Wollongong, Australia.
Professor, Ph.D., Ph.D. adviser, currently the Director of the Center of Applied Superconductivity and Electrical Engineering at the University of Electronic Science and Technology of China. Research interests mainly include applied superconductivity, electromagnetic devices, electric machines, electric power, control, measurement and energy efficiency technology.

You Guang Guo was born in Hubei, China in 1965. He received the B.E. degree from Huazhong University of Science and Technology (HUST), China in 1985, the M.E. degree from Zhejiang University, China in 1988, and the Ph.D. degree from University of Technology, Sydney (UTS), Australia in 2004, all in electrical engineering. His research fields include measurement and modeling of magnetic properties of magnetic materials, numerical analysis of electromagnetic field, electrical machine design and optimization, power electronic drives and control. In these fields, he has published over 230 refereed technical papers including 117 journal articles.

Wei Xu was born in Chongqing, China, in 1980. He received the B.E., B.A., and M.E. degrees from Tianjin University, Tianjin, China, in 2002 and 2005, respectively, and the Ph.D. degree from the Institute of Electrical Engineering, Chinese Academy of Sciences, Beijing, China, in 2008, all in electrical engineering. He is currently a Postdoctoral Fellow with the Center for Electrical Machines and Power Electronics, University of Technology Sydney (UTS), Sydney, Australia, where his research is supported by the Early Career Researcher Grant and partly supported by the Chancellor's Postdoctoral Research Fellowship, both at UTS. His research interests mainly include electromagnetic design and performance analysis of linear/rotary machines, including induction, permanent magnet, switched reluctance, and other emerging novel structure machines.

Hai Yan Lu received the B.E. and M.E. degrees (Electrical Engineering) from Harbin Institute of Technology, China, in 1985 and 1988, respectively, and the Ph.D. degree (Engineering) from University of Technology, Sydney (UTS), Australia, in 2002.
She is currently with the School of Software, Faculty of Engineering and Information Technology, University of Technology, Sydney, Australia. Her research interests include modeling and numerical simulation of magnetic properties of materials, optimal design of electrical machines and drives, heuristic optimisation techniques and intelligent web-based systems. She has published over 50 refereed journal articles and conference papers.

Jian Guo Zhu received his BE in 1982 from Jiangsu Institute of Technology, China, ME in 1987 from Shanghai University of Technology, China, and Ph.D. in 1995 from University of Technology, Sydney (UTS), Australia, He currently holds the positions of Professor of Electrical Engineering and Head for School of Electrical, Mechanical and Mechatronic Systems at UTS, Australia. His research interests include electromagnetics, magnetic properties of materials, electrical machines and drives, power electronics, and renewable energy systems.